

Methods

Data acquisition

We used only FUSE data from the LiF mirror and the A1 detector segment, which have optimal efficiency in the waveband around the O VI line. The data were calibrated and ‘cleaned’ following standard procedures²⁸. The resolution of the final data is $\sim 20 \text{ km s}^{-1}$, at $1,032 \text{ \AA}$.

We selected for our sample only spectra with signal-to-noise ratio (S/N) per resolution element of > 5 at $1,032 \text{ \AA}$ because we were interested in the O VI absorption lines. This selection produced 54 different lines of sight, all with $|b| > 20^\circ$ (because of the high extinction suffered by lines of sight crossing a significant portion of the Galactic disk). In the lowest-quality spectra ($S/N \approx 5$), absorption lines with equivalent width larger than $\sim 200 \text{ m\AA}$ are detected at $> 3\sigma$, whereas the highest S/N spectra in our sample guarantee the detection of absorption lines down to an equivalent width of $\sim 20 \text{ m\AA}$.

Data analysis

For each $z \approx 0$ O VI absorption line spectrum, we used the CIAO fitting engine Sherpa²⁹ to fit a power-law continuum plus negative gaussians to represent the absorption lines, and derived the best-fit wavelengths and widths over $1,028.5 \text{ \AA}$ to $1,034 \text{ \AA}$.

We also looked for possible contamination by H₂ absorption lines from the Galactic interstellar medium, exploiting H₂ templates computed using a non-LTE (local thermodynamic equilibrium) photodissociation front code^{30,31}. The excitation temperatures of the H₂ rotational–vibrational level distribution result from formation pumping, ultraviolet absorption of diffuse ultraviolet starlight in the electronic transitions to the states B, C, B’ and D followed by fluorescence, quadrupole cascading, collisional excitation and de-excitation. Templates have been computed for broad ranges of kinetic temperatures, densities, Doppler parameters and factors of enhancing of the interstellar radiation field. Using these templates, we verified that, in the wavelength range of interest, spectra along lines of sight with equivalent hydrogen column densities lower than $\sim 2 \times 10^{20} \text{ cm}^{-2}$ show only weak H₂ absorption. Spectra along lines of sight with $N_{\text{H}} > 2 \times 10^{20} \text{ cm}^{-2}$, instead, show usually strong (6–0) P(3) $\lambda 1,031.19 \text{ \AA}$ and R(4) $1,032.35 \text{ \AA}$ absorption. The P(3) $\lambda 1,031.19 \text{ \AA}$ and R(4) $1,032.35 \text{ \AA}$ lines occur at velocities of -214 and $+123 \text{ km s}^{-1}$, and so may potentially contaminate HV-O VI lines. We found that about 30% of the negative HV-O VI lines and less than 20% of the positive HV-O VI lines had profiles contaminated by the P(3) $\lambda 1,031.19 \text{ \AA}$ and R(4) $1,032.35 \text{ \AA}$ lines, respectively. For all spectra we used other strong H₂ lines in otherwise relatively featureless portions of the FUSE spectra, to determine the bulk velocity of the H₂ absorber and the strengths of the P(3) $\lambda 1,031.19 \text{ \AA}$ and R(4) $1,032.35 \text{ \AA}$ lines from the relative oscillator strength ratios, allowing us to disentangle the HV-O VI line from the contaminating H₂. In particular, we used the (6–0) P(2) $\lambda 1,028.10 \text{ \AA}$, (6–0) R(3) $\lambda 1,028.98 \text{ \AA}$ and (8–0) P(4) $\lambda 1,012.26 \text{ \AA}$ lines, on the short wavelength side of the O VI $\lambda 1,031.926 \text{ \AA}$ line, and the (5–0) P(2) $\lambda 1,040.36 \text{ \AA}$, (5–0) R(3) $\lambda 1,041.16 \text{ \AA}$ and (5–0) R(4) $\lambda 1,044.54 \text{ \AA}$ lines, on the long wavelength side. Only in two cases could the presence of the HV-O VI line not be safely established, and so we considered those two lines of sight as free from HV-O VI absorption, at our detection threshold. In three more cases the presence of the HV-O VI line was clearly established, but its position and width only poorly constrained.

Cross-correlation

To identify HV-O VI lines with possible HV-H I counterparts, we cross-correlated the objects of our sample with catalogues of 21-cm H I lines^{17,18}. We used very conservative searching criteria, and define a ‘coincidence’ when Galactic coordinates and LSR velocities of the HV-O VI absorbers fall into the very broad ranges (typically tens of degrees and about 100 km s^{-1}) listed in the HV-H I catalogues. The very broad range in coordinates depends, not on the beam-size of the telescope with which 21-cm measurements were performed, but on the entire size of the group or complex of HV-H I clouds to which a given cloud is supposed to belong. This search gave five coincidences. For completeness, we also cross-correlated our coincidences with those found⁴ in the compilation of HV-O VI absorbers¹⁶. This search left only one object. This object has been tentatively associated¹⁶ with the Magellanic stream HV-H I complex, although not with any particular cloud. To be conservative we then add this object to the list of possible OVI-H I identification, and took these six objects off our sample for the purpose of the presented statistical analysis.

Received 16 May; accepted 13 December 2002; doi:10.1038/nature01369.

1. Cen, R. & Ostriker, J. P. Where are the baryons? *Astrophys. J.* **514**, 1–6 (1999).
2. Hellsten, U., Gnedin, N. Y. & Miralda-Escude, J. The X-ray forest: A new prediction of hierarchical structure formation models. *Astrophys. J.* **509**, 56–61 (1998).
3. Davé, R. *et al.* Baryons in the warm-hot intergalactic medium. *Astrophys. J.* **552**, 473–483 (2001).
4. Sembach, K. R. *et al.* Highly-ionized high-velocity gas in the vicinity of the galaxy. *Astrophys. J. Suppl.* (2002) (submitted); preprint astro-ph/0207562 at (<http://xxx.lanl.gov>) (2002).
5. Kahn, F. D. & Woltjer, L. Intergalactic matter and the galaxy. *Astrophys. J.* **130**, 705–717 (1959).
6. Nicastro, F. *et al.* Chandra discovery of a tree in the X-ray forest towards PKS 2155–304: The local filament? *Astrophys. J.* **573**, 157–167 (2002).
7. Canizares, C. R., Schattenburg, M. L. & Smith, H. I. The high energy transmission grating spectrometer for AXAF. *Proc. SPIE* **597**, 253–260 (1986).
8. Moos, H. W. *et al.* Overview of the Far Ultraviolet Spectroscopic Explorer mission. *Astrophys. J.* **538**, L1–L6 (2000).
9. Savage, B. D. *et al.* Far Ultraviolet Spectroscopic Explorer observations of O VI absorption in the galactic halo. *Astrophys. J.* **538**, L27–L30 (2000).
10. Wakker, B. P. *et al.* The FUSE survey of galactic OVI. *Am. Astron. Soc.* **199**, 6508 (2001).
11. Savage, *et al.* Distribution and kinematics of OVI in the Milky Way halo. *Am. Astron. Soc.* **199**, 6504 (2001).
12. Howk, J. C., Savage, B. D., Sembach, K. R. & Hoopes, C. G. Far-Ultraviolet Spectroscopic Explorer observations of degree-scale variations in galactic halo OVI. *Am. Astron. Soc.* **572**, 264–275 (2002).

13. Hoopes, C. G., Sembach, K. R., Howk, J. C., Savage, B. D. & Fullerton, A. W. A Far Ultraviolet Spectroscopic Explorer survey of interstellar OVI absorption in the Small Magellanic Cloud. *Astrophys. J.* **569**, 233–244 (2002).
14. Sembach, K. R. *et al.* Far Ultraviolet Spectroscopic Explorer observations of OVI in high-velocity clouds. *Astrophys. J.* **538**, L31–L34 (2000).
15. Sembach, K. R. High velocity clouds: Cosmological and galactic weather. *Am. Astron. Soc.* **199**, 11301 (2001).
16. Heckman, T. M., Norman, C. A., Strickland, D. K. & Sembach, K. R. On the physical origin of OVI absorption-line systems. *Astrophys. J.* (in the press); preprint astro-ph/020556 at (<http://xxx.lanl.gov>) (2002).
17. Stark, A. A. *et al.* The Bell Laboratories H I survey. *Astrophys. J. Suppl. Ser.* **79**, 77–104 (1992).
18. Wakker, B. P. Distances and metallicities of high- and intermediate-velocity clouds. *Astrophys. J. Suppl. Ser.* **136**, 463–535 (2001).
19. Oort, J. H. Asymmetry in the distribution of stellar velocities. *Observatory* **49**, 302–304 (1926).
20. Kravtsov, A. V., Klypin, A. & Hoffman, Y. Constrained simulations of the real universe: II. Observational signatures of intergalactic gas in the local supercluster region. *Astrophys. J.* (in the press); preprint astro-ph/0109077 at (<http://xxx.lanl.gov>) (2001).
21. Klypin, A., Hoffman, Y., Kravtsov, A. & Gottloeber, S. Constrained simulations of the real universe: The local supercluster. *Astrophys. J.* (2001) (submitted); preprint astro-ph/0107104 at (<http://xxx.lanl.gov>) (2001).
22. Grevesse, N. & Anders, E. *Cosmic Abundances of Matter* (ed. Waddington, C. J.) 1–8 (AIP Conference Proceedings Vol. 183, American Institute of Physics, New York, 1989).
23. Blitz, L., Spergel, D. N., Teuben, P. J., Hartmann, D. & Burton, W. B. High-velocity clouds: Building blocks of the local group. *Astrophys. J.* **514**, 818–843 (1999).
24. Braun, R. & Burton, W. B. The kinematic and spatial deployment of compact, isolated high-velocity clouds. *Astrophys. J.* **341**, 437–450 (1999).
25. Braun, R. & Burton, W. B. Status of HI searches for CHVCs beyond the local group. *Astron. Astrophys.* **375**, 219–226 (2001).
26. de Heij, V., Braun, R. & Burton, W. B. An all-sky study of compact isolated high velocity clouds. *Astron. Astrophys.* (in the press); preprint astro-ph/0206306 at (<http://xxx.lanl.gov>) (2002).
27. Sternberg, A., McKee, C. F. & Wolfire, M. G. Atomic hydrogen gas in dark-matter minihalos and the compact high velocity clouds. *Astrophys. J. Suppl.* (2002) (in the press); preprint astro-ph/0207040 at (<http://xxx.lanl.gov>) (2002).
28. Sankrit, R., Kruk, J. W., Ake, T. B. & Anderson B.-G. *The FUSE Data Analysis Cookbook v. 1.0* (<http://fuse.pha.jhu.edu/analysis.cookbook.html>) (2001).
29. Freeman, P., Doe, S. & Siemiginowska, A. Sherpa: A mission-independent data analysis application. *Proc. SPIE* **4477**, 76–87 (2001).
30. Draine, B. T. & Bertoldi, F. Structure of stationary photodissociation fronts. *Astrophys. J.* **468**, 269–289 (1996).
31. Cecchi-Pestellini, C., Casu, S. & Dalgarno, A. The population of the high H₂ rotational states towards the OMC-1 peak 1. *Astrophys. J.* (submitted).

Acknowledgements F.N. thanks P. Kaaret and G. C. Perola for discussions and comments. We thank W.B. Burton for comments that helped improve the Letter. This work was partly supported by NASA-Chandra grants and a NASA-Chandra X-ray Center contract.

Competing interests statement The authors declare that they have no competing financial interests.

Correspondence and requests for materials should be addressed to F.N. (e-mail: fnicastro@cfa.harvard.edu).

Experimental realization of freely propagating teleported qubits

Jian-Wei Pan, Sara Gasparoni, Markus Aspelmeyer, Thomas Jennewein & Anton Zeilinger

Institut für Experimentalphysik, Universität Wien, Boltzmanngasse 5, 1090 Wien, Austria

Quantum teleportation¹ is central to quantum communication, and plays an important role in a number of quantum computation protocols^{2,3}. Most information-processing applications of quantum teleportation include the subsequent manipulation of the qubit (the teleported photon), so it is highly desirable to have a teleportation procedure resulting in high-quality, freely flying qubits. In our previous teleportation experiment⁴, the teleported qubit had to be detected (and thus destroyed) to verify the success of the procedure. Here we report a teleportation experiment that results in freely propagating individual qubits. The basic idea is to suppress unwanted coincidence detection events by providing

the photon to be teleported much less frequently than the auxiliary entangled pair. Therefore, a case of successful teleportation can be identified with high probability without the need actually to detect the teleported photon. The experimental fidelity of our procedure surpasses the theoretical limit required for the implementation of quantum repeaters^{5,6}.

To see how to achieve free propagation of teleported qubits, we first briefly review the working principle of the earlier Innsbruck teleportation experiment as illustrated in Fig. 1a. Suppose photon 1, which Alice wants to teleport to Bob, is in a general polarization state $|\Phi\rangle_1 = \alpha|H\rangle_1 + \beta|V\rangle_1$ (unknown to Alice), and the pair of photons 2 and 3 shared by Alice and Bob is in the polarization entangled state $|\Phi^+\rangle_{23}$. We use the usual Bell states:

$$|\Phi^\pm\rangle_{ij} = \frac{1}{\sqrt{2}}(|H\rangle_i|H\rangle_j \pm |V\rangle_i|V\rangle_j)$$

$$|\Psi^\pm\rangle_{ij} = \frac{1}{\sqrt{2}}(|H\rangle_i|V\rangle_j \pm |V\rangle_i|H\rangle_j) \quad (1)$$

where *H* and *V* denote horizontal and vertical linear polarizations, and *i* and *j* index the spatial modes of the photons. We choose the state $|\Phi^+\rangle_{23}$ just for the convenience of discussion. The overall state of photons 1, 2 and 3 can then be rewritten as:

$$|\Psi\rangle_{123} = |\Phi\rangle_1|\Phi^+\rangle_{23}$$

$$= \frac{1}{2}[|\Phi^+\rangle_{12}(\alpha|H\rangle_3 + \beta|V\rangle_3) + |\Phi^-\rangle_{12}(\alpha|H\rangle_3 - \beta|V\rangle_3)$$

$$+ |\Psi^+\rangle_{12}(\alpha|V\rangle_3 + \beta|H\rangle_3) + |\Psi^-\rangle_{12}(\alpha|V\rangle_3 - \beta|H\rangle_3)] \quad (2)$$

It can thus be seen that a joint Bell measurement on photons 1 and 2 at Alice's side projects the state of photon 3 at Bob's side into one of the four corresponding states as shown in equation (1). Depending on Alice's measurement results, Bob can then perform a unitary transformation, independent of $|\Phi\rangle_1$, on photon 3 to convert its state into the initial state of photon 1. This is how quantum teleportation works. Obviously, to demonstrate the working principle of teleportation it is sufficient to identify one of the four Bell-states. This results in a reduced efficiency—the fraction of success—of 25%. In the Innsbruck experiment, this is accomplished by detecting a twofold coincidence behind a 50:50 beamsplitter.

So far, we considered only the ideal case where there is one and only one photon pair in each of the pairs of modes 1-4 and 2-3. Then it is clear that a threefold coincidence of detectors D1-D2-T is enough to guarantee a successful teleportation. However, because of the probabilistic feature of pair creation in spontaneous parametric down-conversion (SPDC), this conclusion cannot be applied to the Innsbruck experiment.

To see the problem more clearly, let us denote by *p* the probability of having a single pair creation during a SPDC process. For independent probabilistic pair creation the probability of having one photon pair in each of the pairs of modes 1-4 and 2-3, which corresponds to a successful teleportation event, is then given by *p*². Yet sometimes two pairs of photons are both emitted into either modes 1-4 or 2-3. Specifically, with the probability of *p*² the two photon pairs could both appear in modes 1-4 while no photons are present in modes 2-3. In this case, although a threefold coincidence of D1, D2 and T is detected, no teleportation occurs because of the absence of the entangled pair in modes 2-3 and mode 3 is simply empty. To ensure a successful teleportation, it is therefore necessary in the Innsbruck experiment to confirm the presence of photon 3 by actually detecting it. For this reason, the Innsbruck experiment has been called a "postselected" one⁷; using the word "conditional" would be more appropriate as photon 3 is not selected depending on its state⁸.

Most applications of quantum teleportation include the subsequent manipulation of the teleported photon. Thus, a freely

propagating output state, which is teleported with high fidelity, is strongly desired. This calls for a non-conditional qubit teleportation scheme. Possible solutions^{7,9} could include the discrimination of one- and two-photon events at detector T, a quantum non-demolition measurement of the photon number in mode 3, or the introduction of an unbalanced coupling between modes 1-4 relative to modes 2-3. But owing to the lack of appropriate technology, none of the proposed schemes has so far been realized.

In other experimental efforts^{10,11} to achieve full teleportation, other problems still remain for various reasons. Concerning the case of continuous variable teleportation¹⁰, criticism has been raised due to the low fidelity¹² and the need of a phase reference¹³. In the other case¹¹, the input state fails to meet the criterion of being a quantum state, since about 10⁵ photons are prepared in the input beam.

In the present experiment, we achieve a freely propagating teleported quantum state by making a detection at Bob's side obsolete (Fig. 1b). The main point is to reduce the number of unwanted D1-D2 coincidence counts. This is accomplished by attenuating the beam 1 by a factor of γ while leaving the other modes unchanged. Then a threefold coincidence D1-D2-T will occur with probability γp^2 owing to successful teleportation and with significantly lower probability $(\gamma p)^2$ they will be a spurious coincidence. Thus, for sufficiently low γ it will no longer be necessary to actually detect the teleported photon 3 and a freely propagating teleported beam of qubits emerges. In essence, we provide the entangled ancillary pair more frequently than the photon to be teleported. Thus it can only very rarely happen that

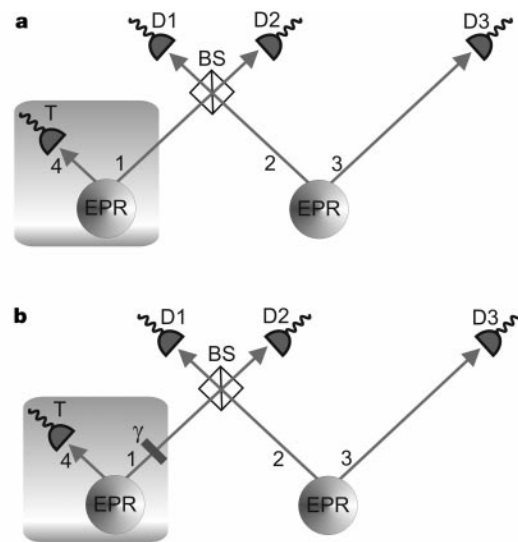


Figure 1 Diagrams showing the principles of the Innsbruck experiment and of achieving free propagation of teleported qubits. **a**, The Innsbruck experiment. Two independent polarization entangled photon pairs produced by spontaneous parametric down-conversion (SPDC) are used to achieve quantum teleportation. While the first pair (photons 2 and 3) provides the entangled pair needed in the teleportation protocol, the second pair (photons 1 and 4) is used to prepare the initial state to be teleported. The 'twin' photon 4 acts only as a trigger. In the case where one pair of photons is emitted in each of the pairs of modes 1-4 and 2-3, a threefold coincidence of T-D1-D2 is enough to indicate a successful teleportation. However, in the case where both photon pairs are emitted into modes 1-4, threefold coincidences of T-D1-D2 also result. In that case, no teleportation occurs because mode 3 is simply empty. Therefore detection of the teleported photon 3 is needed to rule out this bad case. **b**, Free propagation of teleported qubits. An additional attenuator is inserted into mode 1 to decrease the probability of unwanted, spurious threefold coincidence detection events of D1-D2-T resulting from double-pair emission into modes 1-4. This method makes a detection at Bob's side obsolete and leads to free propagation of teleported qubits (see text). EPR, Einstein-Podolsky-Rosen entangled photon sources. BS, beamsplitter. D1, D2 and T, detectors.

the teleportation machinery is not ready when a photon arrives to be teleported.

A schematic drawing of the experimental set-up is shown in Fig. 2. As in our recent experimental demonstration of four-photon entanglement¹⁴, we exploit a polarizing beamsplitter (PBS) instead of a normal beamsplitter to perform the necessary Bell-state measurement. In the experiment, we prepared the entangled pair in state $|\Phi^+\rangle_{23}$ and chose to analyse the projection onto state $|\Phi^+\rangle_{12}$. This projection can be accomplished by performing a joint polarization measurement in the 45° basis behind the PBS. As stated in ref. 15, registering $+45^\circ/+45^\circ$ or $-45^\circ/-45^\circ$ coincidences of detectors D1 and D2 acts as a projection onto $|\Phi^+\rangle_{12}$. This projection leaves photon 3 in the initial state (see equation (2)).

Here we emphasize that one can neglect the cases where a single pair production in modes 1-4 and a double pair production in modes 2-3 give rise to third-order spurious coincidences with probability p^3 . This is because in our experiment $\gamma \gg p$. Therefore, such third-order spurious coincidences are at most one-tenth of those contributed from the double pair emission in modes 1-4, and are even much smaller than the good coincidence events. In that sense, our scheme to attenuate the beam 1 is equivalent to the one to attenuate the reflected pump beam as suggested in ref. 9.

A high-intensity source of entangled photon pairs is desirable to collect enough experimental data within a reasonably short time, because the method of beam attenuation significantly reduces the overall fourfold coincidences (typically by one order of magnitude). Various efforts have been made to achieve this purpose. By using a compact set-up and by focusing the ultraviolet (UV) pump (with a beam diameter <0.5 mm) onto the beta-barium borate (BBO) crystal, we achieved both better stability and collection efficiency. We thus managed to observe about 2×10^4 entangled photon pairs per second, while achieving a high twofold visibility of 94% in the 45° basis. Correspondingly, the observed overall fourfold coincidence rate was as high as two per second on average, which is almost two orders of magnitude higher than recent work in quantum teleportation^{14,16}. Note that high multi-fold coincidences have

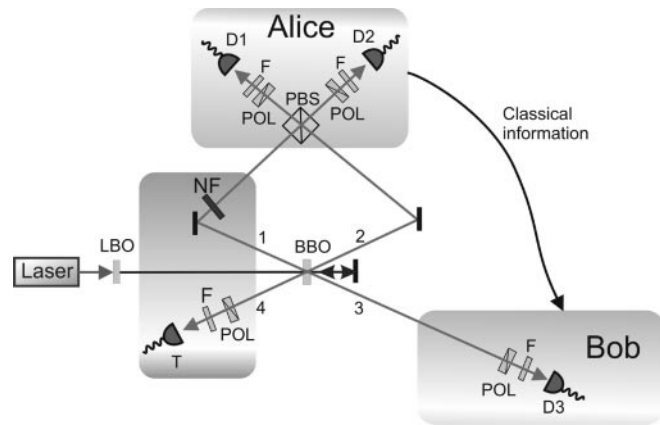


Figure 2 Set-up for experimental demonstration of free propagation of teleported qubits. A mode-locked laser produces pulses of 200 fs with a repetition rate of 76 MHz, centred on the wavelength of 788 nm. This radiation is used to pump an up-conversion process in an LBO and the outgoing radiation is further sent to a BBO crystal. Two independent EPR pairs are produced through SPDC, the first during the direct passage of the pump light (2 and 3), and the second during its back propagation (1 and 4). A polarizer (POL) is put in front of the trigger detector T to prepare photon 1 nonlocally in the state to be teleported. Various neutral filters (NF) are inserted into beam 1 to achieve the required attenuation. Photons 1 and 2 are then steered to a polarizing beamsplitter (PBS) to perform the necessary Bell-state measurement. To ensure good temporal and spatial overlap of the two photons, the two outputs of the PBS are spectrally filtered (3-nm bandwidth) and monitored by fibre-coupled single photon detectors. LBO, lithium triborate crystal. F, narrow bandwidth filters.

also been observed in very different experiments^{17,18}.

To experimentally demonstrate non-conditional teleportation, we inserted a series of neutral filters in mode 1 and showed that the probability of having a successful teleportation dependent on a threefold coincidence of D1, D2 and T increases with decreasing filter transmission γ .

First, we performed teleportation of a 45° polarized photon. The state to be teleported was prepared nonlocally by using the entanglement of photons 1 and 4. In the experiment, both the threefold coincidences C_3 of D1, D2 and T and the fourfold coincidences C_4 of all outputs were measured. As an example, the measurement results for the case of $\gamma = 1$ (that is, no attenuation) is shown in Fig. 3a. It is obvious that the observed probability to have a successful teleportation once a threefold coincidence occurs is given by C_4/C_3 . Owing to the finite detection efficiency η_3 of D3, only a fraction of the total successful teleportation events will be registered by detector D3. This implies that the genuine probability of success is given by the observed probability of success divided by the detection efficiency, that is $C_4/(C_3\eta_3)$.

Measuring C_3 , C_4 and η_3 (typically 0.15), we can thus obtain the observed and genuine probabilities to have a successful teleportation, based on a threefold coincidence, for different neutral filters. Table 1 summarizes the experimental results in our 45° teleportation experiment. The experimental results well confirm,

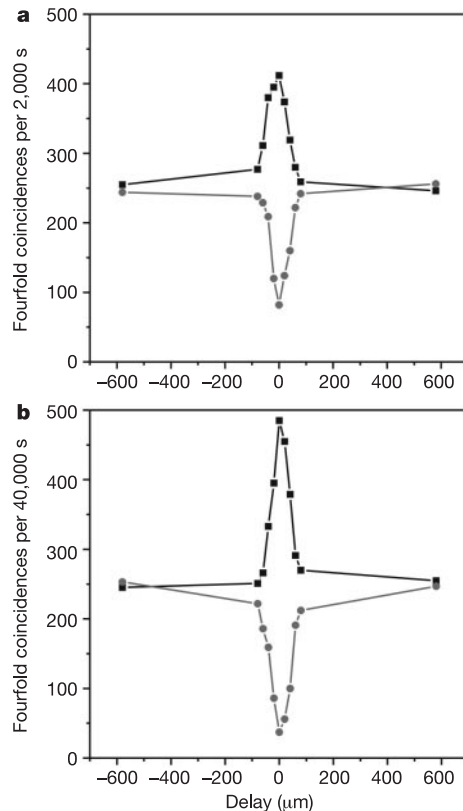


Figure 3 Two typical experimental results for 45° teleportation. **a**, Fourfold coincidences between the detectors T, D1, D2 and D3 as a function of time delay between the arrival of photons 1 and 2 at the PBS. Shown are the cases where the polarizer in front of D3 is set to 45° (square) and -45° (circle). At large delay, no two-photon interference between photons 1 and 2 occurs, and therefore the polarization correlation between photons 1 and 3 is completely random. At zero delay a perfect overlap between photons 1 and 2 leads to a successful projection onto $|\Phi^+\rangle_{12}$ and results in teleportation of the input state $|\Phi^+\rangle_1$. The data shown were measured without using neutral filters and before birefringence compensation. **b**, The experimental visibility is drastically enhanced from 66% to 86% after birefringence compensation. Note that in this measurement, one neutral filter with $\gamma = 0.05$ was used just to obtain the unbalancing.

Table 1 Probabilities of success for different filters

Attenuation	Observed	Genuine
1	0.060 ± 0.001	0.40 ± 0.01
0.50	0.079 ± 0.001	0.53 ± 0.01
0.10	0.119 ± 0.002	0.79 ± 0.01
0.05	0.138 ± 0.002	0.92 ± 0.01

in agreement with our above analysis, that the probability of success increases with decreasing γ . Note that for a given γ all data points in scan (Fig. 3) are used to estimate the probability of success, which results in a small statistical error.

Using the product of the measured fidelities and probabilities of a successful teleportation, we can obtain the non-conditional fidelity. The corresponding fidelities are shown in Fig. 4 for the conditional detection scheme and for the new unbalanced interferometer scheme at different grades of attenuation. If no attenuation is used the set-up is in principle equivalent to the original Innsbruck scheme and the freely propagating output state fully incorporates the vacuum contribution, resulting in a non-conditional fidelity below the classical limit. With increasing attenuation ('unbalancing') the vacuum contribution can be suppressed, resulting in a higher non-conditional fidelity. For the case where an attenuation factor of $\gamma = 0.05$ is chosen, the experimental non-conditional fidelity is 0.79 ± 0.02 , which significantly overcomes the classical limit of two-thirds.

For a complete demonstration of our teleportation method, in the experiment we also teleported photons with horizontal linear polarization (that is, H) and right-handed circular polarization (that is, R), thus demonstrating the scheme for three orthogonal directions on the Poincaré sphere. The non-conditional fidelities measured for different preparation bases are summarized in Table 2. We conclude that in all three cases the obtained non-conditional fidelities are well above the classical limit. We noticed that, whereas both the 45° and R teleportation experiments have roughly the same fidelities, a much better fidelity is obtained in the H teleportation experiment. This is because we chose the H - V direction as the intrinsic measurement basis of the polarizing beamsplitter cube and so the direction of polarization is aligned with respect to the optical axes. All input pairs of H or V polarization only collect an overall phase and are thus, in the case of projection onto a $|\Phi^+\rangle$ -state, always directed into different beamsplitter outputs. For the case of arbitrary polarized

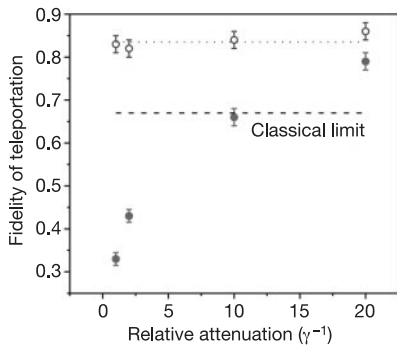


Figure 4 Conditional fidelities and non-conditional fidelities obtained in 45° teleportation for different neutral filters. With increasing attenuation of the beam 1, we observe an increase of non-conditional fidelities (black symbols) while the conditional ones (open symbols) remain constant. In the experiment, the integration times for various γ were, respectively, about 2×10^3 , 4×10^3 , 2×10^4 and 4×10^4 s per measurement point on the average. For each γ we collected about 400 fourfold counts for peak and 80 for dip. For $\gamma = 0.10$, the classical limit is already reached, and for $\gamma = 0.05$ it is clearly overcome, resulting in freely propagating teleported photon states of high fidelity.

Table 2 Fidelities of non-conditional teleportation

Polarization	$\gamma = 1$	$\gamma = 0.05$
45°	0.35 ± 0.02	0.79 ± 0.02
H	0.39 ± 0.02	0.84 ± 0.02
R	0.34 ± 0.02	0.76 ± 0.02

input states, an additional phase difference between horizontal and vertical components is introduced in the $|\Phi\rangle$ -states, which consequently leads to a reduction of teleportation fidelity.

However, we can introduce an additional birefringent element in order to compensate for the above effect. After this compensation, as a test, we repeated the 45° teleportation experiment for the cases of $\gamma = 1$ and $\gamma = 0.05$. The experimental result for $\gamma = 0.05$ is shown in Fig. 3b. The compensation of birefringence effects in the experimental set-up increases the non-conditional fidelity in the 45° teleportation from 0.79 ± 0.02 to 0.85 ± 0.02 , which is compatible with that obtained in our H teleportation. This improvement implies that the PBS accuracy of interfering two independent photons has been raised from 89% to 97%, which is the fidelity of the Bell-state measurement of $|\Phi^+\rangle$. This is obtained from the experimental visibility for 45° teleportation after taking into account the imperfection of the state preparation. We emphasize that such a high accuracy achieved in the present experiment now fulfills the strict precision requirements of 95% for local operations of independent photons necessary for quantum repeaters in long-distance quantum communication^{5,6}.

We were thus able to demonstrate the preparation of a freely propagating teleported quantum state with high (non-conditional) fidelity of 0.85 ± 0.02 , that is, well above the classical limit. Our present results also confirm that the Innsbruck experiment was a bona fide realization of quantum teleportation. Furthermore, together with the expected future realization of entanglement purification^{19,20}, the high experimental visibility obtained will allow the next step towards long-distance quantum communication. □

Received 26 September; accepted 30 December 2002; doi:10.1038/nature01412.

- Bennett, C. H. et al. Teleporting an unknown quantum state via dual classical and Einstein-Podolsky-Rosen channels. *Phys. Rev. Lett.* **83**, 3081–3084 (1993).
- Gottesman, D. & Chuang, I. L. Demonstrating the viability of universal quantum computation using teleportation and single-qubit operations. *Nature* **402**, 390–393 (1999).
- Knill, E., Laflamme, R. & Milburn, G. J. A scheme for efficient quantum computation with linear optics. *Nature* **409**, 46–52 (2001).
- Bouwmeester, D. et al. Experimental quantum teleportation. *Nature* **390**, 575–579 (1997).
- Briegleb, H.-J., Duer, W., Cirac, J. I. & Zoller, P. Quantum repeaters: The role of imperfect local operations in quantum communication. *Phys. Rev. Lett.* **81**, 5932–5935 (1998).
- Aschauer, H. & Briegel, H. J. Private entanglement over arbitrary distances, even using noisy apparatus. *Phys. Rev. Lett.* **88**, 047902 (2002).
- Braunstein, S. L. & Kimble, H. J. A posteriori teleportation. *Nature* **394**, 840–841 (1998).
- Bouwmeester, D. et al. Reply to "A posteriori teleportation". *Nature* **394**, 841 (1998).
- Kok, P. & Braunstein, S. L. Postselected versus nonpostselected quantum teleportation using parametric down-conversion. *Phys. Rev. A* **61**, 042304 (2000).
- Furusawa, A. et al. Unconditional quantum teleportation. *Science* **282**, 706–709 (1998).
- Kim, Y. H., Kulik, S. P. & Shih, Y. H. Quantum teleportation of a polarization state with a complete Bell state measurement. *Phys. Rev. Lett.* **86**, 1370–1373 (2001).
- Grosshans, F. & Grangier, P. Quantum cloning and teleportation criteria for continuous quantum variables. *Phys. Rev. A* **64**, R010301 (2001).
- Rudolph, T. & Sanders, B. C. Requirement of optical coherence for continuous variable quantum teleportation. *Phys. Rev. Lett.* **88**, 077903 (2001).
- Pan, J.-W. et al. Experimental demonstration of four-photon entanglement and high-fidelity teleportation. *Phys. Rev. Lett.* **86**, 4435–4438 (2001).
- Pan, J.-W. & Zeilinger, A. Greenberger-Horne-Zeilinger-state analyzer. *Phys. Rev. A* **57**, 2208–2211 (1998).
- Jennewein, T., Weihs, G., Pan, J.-W. & Zeilinger, A. Experimental nonlocality proof of quantum teleportation and entanglement swapping. *Phys. Rev. Lett.* **88**, 017093 (2002).
- Kurtsiefer, C., Oberparleiter, M. & Weinfurter, H. High-efficiency entangled photon pair collection in type-II parametric fluorescence. *Phys. Rev. A* **64**, 023802 (2001).
- Howell, J. C., Lamas-Linares, A. & Bouwmeester, D. Experimental violation of a spin-1 Bell inequality using maximally entangled four-photon states. *Phys. Rev. Lett.* **88**, 030401 (2002).
- Bennett, C. H. et al. Purification of noisy entanglement, and faithful teleportation via noisy channel. *Phys. Rev. Lett.* **76**, 1895–1898 (1996).
- Pan, J.-W., Simon, C., Brukner, C. & Zeilinger, A. Entanglement purification for quantum communication. *Nature* **410**, 1067–1070 (2001).

Acknowledgements This work was supported by the Austrian Science Foundation (FWF), the TMR and the QuComm programmes of the European Commission and the Alexander von Humboldt Foundation.

Competing interests statement The authors declare that they have no competing financial interests.

Correspondence and requests for materials should be addressed to J.-W.P. (e-mail: pan@ap.univie.ac.at) or A.Z. (e-mail: Zeilinger-office@exp.univie.ac.at).

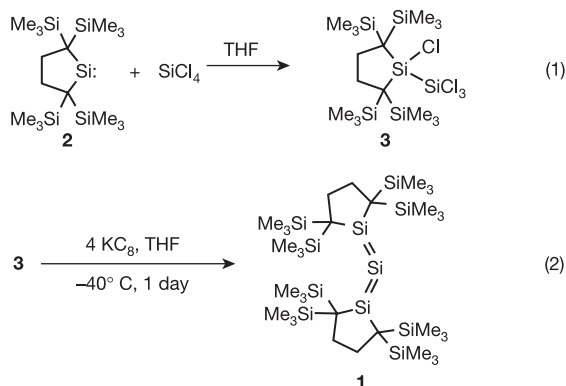
A stable silicon-based allene analogue with a formally *sp*-hybridized silicon atom

S. Ishida, T. Iwamoto, C. Kabuto & M. Kira

Department of Chemistry, Graduate School of Science, Tohoku University, Aoba-ku, Sendai 980-8578, Japan

Carbon chemistry exhibits a rich variety in bonding patterns, with homo- or heteronuclear multiple bonds involving *sp*-hybridized carbon atoms as found in molecules such as acetylenes, nitriles, allenes and carbon dioxide. Carbon's heavier homologues in group 14 of the periodic table—including silicon, germanium and tin—were long thought incapable of forming multiple bonds because of the less effective $p\pi-p\pi$ orbital overlap involved in the multiple bonds. However, bulky substituents can protect unsaturated bonds and stabilize compounds with formally *sp*-hybridized heavy group-14 atoms^{1,2}: stable germanium², tin³ and lead⁴ analogues of acetylene derivatives and a marginally stable tristannaallene⁵ have now been reported. However, no stable silicon compounds with formal *sp*-silicon atoms have been isolated. Evidence for the existence of a persistent disilaacetylene⁶ and trapping⁷ of transient 2-silaallenes and other $X=Si=X'$ type compounds ($X, X' = O, CR_2, NR$, and so on) are also known, but stable silicon compounds with formally *sp*-hybridized silicon atoms have not yet been isolated. Here we report the synthesis of a thermally stable, crystalline trisilaallene derivative containing a formally *sp*-hybridized silicon atom. We find that, in contrast to linear carbon allenes, the trisilaallene is significantly bent. The central silicon in the molecule is dynamically disordered, which we ascribe to ready rotation of the central silicon atom around the molecular axis.

Trisilaallene **1** was prepared as a green solid using two-step reactions from silylene **2** (ref. 8) in overall 42% yield (equations (1) and (2)). Trisilaallene **1** is sensitive to air but is thermally rather



stable with a melting point of 198–200 °C. The structure of **1** was determined by ¹H, ¹³C, and ²⁹Si NMR spectroscopy and X-ray

crystallography (see Supplementary Information for details).

X-ray single crystal analysis shows a quite unusual structural feature of trisilaallene **1** (Fig. 1). In contrast to carbon allenes, the trisilaallene skeleton is not linear but bent. The central silicon atom (Si^2) in the crystal was found at four positions labelled Si^{2A} to Si^{2D} in Fig. 1a at higher temperatures than -100 °C, indicating that four structurally similar isomers exist, A to D. The populations for A to D are independent of crystals but are significantly temperature-dependent: the populations are 46, 23, 22 and 10% at 0 °C, but 76, 18, 7 and 0% at -150 °C, respectively (see Supplementary Information for details). The energy differences between isomers A to D are estimated to be within 1 kcal mol^{-1} , suggesting a dynamic disorder⁹ mediated by a rotation of the Si^2 atom around the Si^1-Si^3 axis.

The details of the molecular structure of isomer A of trisilaallene **1** at -150 °C are as follows: (1) The $Si^1=Si^2=Si^3$ skeleton is not linear but is significantly bent with a bond angle of $136.49(6)^\circ$ (standard deviation is in parentheses), indicating that the bonding at Si^2 atom cannot be described by using simple *sp*-hybridization any longer. (2) The two $Si=Si$ bond lengths in **1** (2.177(1) and 2.188(1) Å) are in the range of those for typical stable disilenes (2.14–2.29 Å). (3) The two five-membered rings are almost perpen-

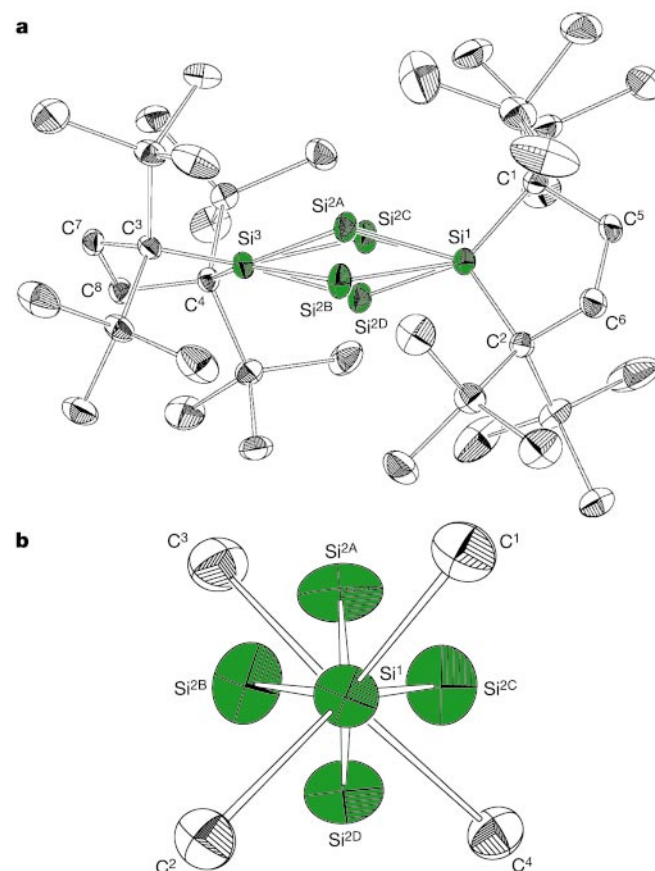


Figure 1 Molecular structure of trisilaallene **1** at -50 °C. **a**, A top view (hydrogen atoms were omitted for clarity). **b**, A side view ($C_2Si^1=Si^2=Si^3C_2$ skeleton). As shown in **b**, $Si^{2A}-Si^{2D}$ are found in four quadrants divided by two perpendicular planes of $C^1-Si^1-C^2$ and $C^3-Si^3-C^4$, respectively. The environments of the four quadrants are slightly different from each other owing to the non-planarity of the five-membered rings, and hence, the occupancies of $Si^{2A}-Si^{2D}$ are not equal to each other. X-ray analysis for two different single crystals of **1** showed that the populations are independent of the crystals but are significantly temperature-dependent. The populations of isomers **A** to **D** are: 53, 22, 19 and 7% at -50 °C and 76, 18, 7 and 0% at -150 °C for crystal 1; 46, 23, 22 and 10% at 0 °C; 52, 22, 19 and 7% at -50 °C; 61, 21, 15 and 4% at -100 °C; and 72, 19, 10 and 0% at -146 °C for crystal 2.